Tunable Coupling and Isolation of Single Electrons in Silicon Metal-Oxide-Semiconductor Quantum Dots

Eenink, H. G.J.; Petit, L.; Lawrie, W. I.L.; Clarke, J. S.; Vandersypen, L. M.K.; Veldhorst, M.

DOI
10.1021/acs.nanolett.9b03254

Publication date
2019

Document Version
Final published version

Published in
Nano Letters

NANO LETTERS
Letter
Cite This: Nano Lett. 2019, 19, 8653−8657
pubs.acs.org/NanoLett

Tunable Coupling and Isolation of Single Electrons in Silicon Metal-Oxide-Semiconductor Quantum Dots

H. G. J. Eenink,[†,§] L. Petit,[†,§] W. I. L. Lawrie,[†] J. S. Clarke,[‡] L. M. K. Vandersypen,[†] and M. Veldhorst*[,†]

[†]QuTech and Kavli Institute of Nanoscience, TU Delft, P.O. Box 5046, 2600 GA Delft, The Netherlands
[‡]Components Research, Intel Corporation, 2501 Northeast Century Boulevard, Hillsboro, Oregon 97124, United States

Supporting Information

ABSTRACT: Extremely long coherence times, excellent single-qubit gate fidelities, and two-qubit logic have been demonstrated with silicon metal-oxide-semiconductor spin qubits, making it one of the leading platforms for quantum information processing. Despite this, a long-standing challenge in this system has been the demonstration of tunable tunnel coupling between single electrons. Here we overcome this hurdle with gate-defined quantum dots and show couplings that can be tuned on and off for quantum operations. We use charge sensing to discriminate between the (2,0) and (1,1) charge states of a double quantum dot and show excellent charge sensitivity. We demonstrate tunable coupling up to 13 GHz, obtained by fitting charge polarization lines, and tunable tunnel rates down to <1 Hz, deduced from the random telegraph signal. The demonstration of tunable coupling between single electrons in a silicon metal-oxide-semiconductor device provides significant scope for high-fidelity two-qubit logic toward quantum information processing with standard manufacturing.

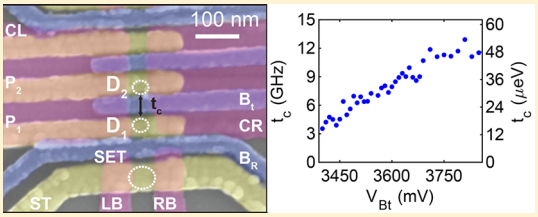

KEYWORDS: *Silicon, tunnel coupling, quantum dots*

Quantum computation with quantum dots has been proposed using qubits defined on the spin states of one,[1] two,[2] or more[3,4] electrons. In all of these proposals, a crucial element required to realize a universal quantum gate set is the exchange interaction between electrons. The exchange interaction is set by the tunnel coupling and the detuning, and gaining precise control over these parameters enables us to define and operate qubits at their optimal points.[5−8] Excellent control has already been reported in GaAs,[5,6,9] strained silicon,[10,11] and, more recently, strained germanium.[12,13] Reaching this level of control in silicon metal-oxide-semiconductor (SiMOS) quantum dots is highly desired because this platform has a high potential for complete integration with classical manufacturing technology.[14−16] This becomes apparent from many proposals of architectures for large-scale quantum computation[1,17−22] that make use of full control over the exchange interaction. However, the current two-qubit logic with single spins in SiMOS is based on controlling the exchange using the detuning only[23] or is executed at a fixed exchange interaction.[24]

A first step toward the required control has been the demonstration of tunable coupling in a double quantum dot system operated in the many-electron regime, where gaining control is more accessible owing to the larger electron wave function.[25,26] More recently, exchange-controlled two-qubit operations have been shown with three-electron quantum dots.[27] However, tunnel couplings between single electrons that can be switched off and turned on for qubit operation still remain to be shown in SiMOS.

In this work, we show a high degree of control over the tunnel coupling of single electrons residing in two gate-defined quantum dots in a SiMOS device. The system is stable, and no unintentional quantum dots are observed. We are able to measure charge transitions using a sensitive single-electron transistor (SET) as a charge sensor and characterize the system in the single-electron regime. From a comparison of charge stability diagrams of weakly and strongly coupled double quantum dots, we conclude that we control the tunnel coupling by changing the quantum dot location. We show that we can effectively decouple the double quantum dot from its reservoir and control the interdot tunnel coupling of the isolated system with a dedicated barrier gate. We quantify the tunability of the coupling by analyzing charge polarization lines and random telegraph signals (RTSs) and find tunnel couplings up to 13 GHz and tunnel rates down to <1 Hz.

Results and Discussion. Figure 1a shows a scanning electron micrograph (SEM) of a SiMOS device nominally identical to the one measured, and Figure 1b shows a schematic cross-section of the quantum dot region along the dashed line in Figure 1a. A high-quality wafer is realized[14] with a 100 nm ^{28}Si epilayer with an 800 ppm residual ^{29}Si concentration,[28] covered by 10 nm thermally grown SiO_2. Ohmic contacts are made by defining highly doped n^{++} regions by phosphorus-ion

Received: August 8, 2019
Revised: November 7, 2019
Published: November 22, 2019

DOI: 10.1021/acs.nanolett.9b03254
Nano Lett. 2019, 19, 8653−8657

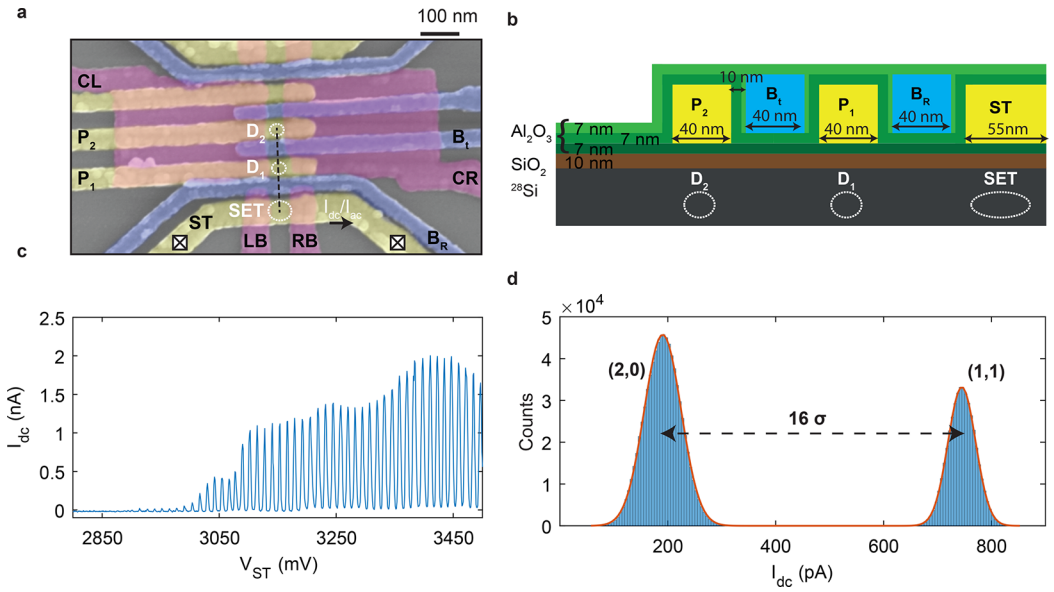

Figure 1. Device layout and SET characterization. (a) False-color scanning electron micrograph (SEM) of a device identical to the one measured. Purple, yellow, and blue correspond to the first, second, and third metal layers, respectively. Crossed boxes indicate the ohmic source and drain contacts used to measure I_{dc} and I_{ac}, and circles indicate the intended location of the quantum dots D_1 and D_2 and the single-electron transistor (SET). The quantum dots are defined using gate electrodes P_1 and P_2, confined laterally using CL and CR. B_t controls the tunnel coupling between the quantum dots, and B_R controls the tunnel coupling to the SET. (b) Schematic of a cross-section of the device along the quantum dot region (dashed line in panel a), indicating key dimensions and dot locations. (c) Transport source-drain current I_{dc} versus top-gate voltage V_{ST} of the SET defined using gate electrodes ST, LB, and RB. The regular spacing of Coulomb peaks indicates a well-defined quantum dot, ideal for charge sensing. (d) Histogram of the charge sensor current as a response to (2,0)-(1,1) tunneling events. The counts are extracted from 4655 single-shot traces with integration time $t_i = 82\ \mu s$, measurement bandwidth 0−50 kHz, and bin size $b = 5$ pA. The peaks are fitted with a double Gaussian with $\sigma_{(2,0)} = 34.1$ pA and $\sigma_{(1,1)} = 25.5$ pA, giving a peak spacing of $>16\sigma_{(2,0)}$.

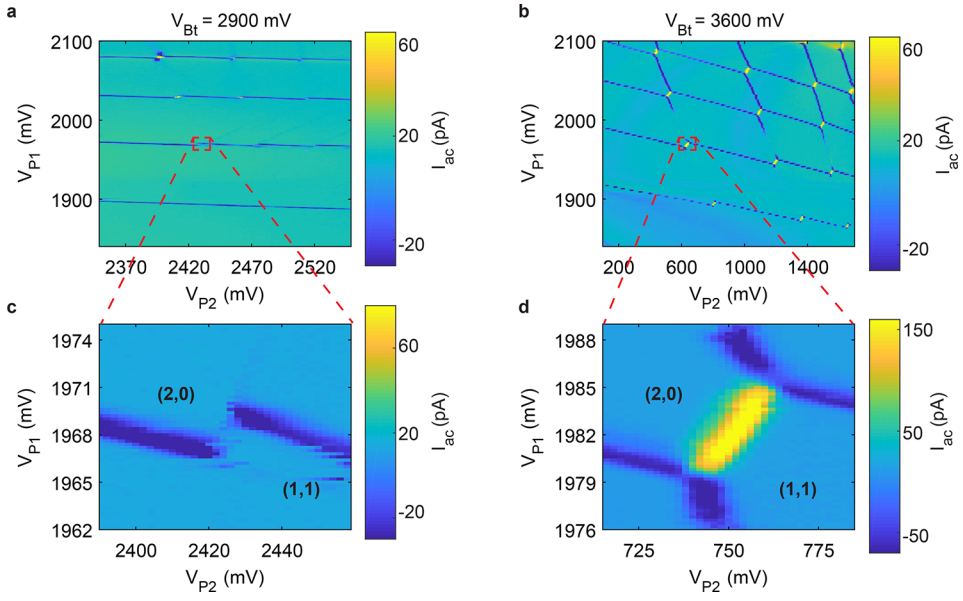

Figure 2. Double quantum dot charge stability diagrams. (a,b) Charge stability diagrams of the charge sensor response I_{ac} as a function of voltages V_{P_2} and V_{P_1} of a double quantum dot for weak ((a) $V_{B_t} = 2.9$ V) and strong ((b) $V_{B_t} = 3.6$ V) coupling. Electrons are loaded from the SET. Transitions with a tunnel rate $\Gamma < f_{ac}$ are not visible. (c,d) High-resolution zoom-in of the (2,0)-(1,1) anticrossing for both (c) weak and (d) strong tunnel coupling.

implantation. We use an overlapping gate integration scheme[10,29,30] and use palladium (Pd) gates, which have the beneficial property of small grain size.[31] The gates are electrically isolated by an Al_2O_3 layer grown by atomic layer deposition. The sample is annealed at 400 °C in a hydrogen atmosphere to repair the e-beam induced damage to the silicon oxide and to reduce the charge trap density.[32,33]

Figure 1c shows the current through the SET, electrostatically defined using gates ST, LB, and RB, that is used as a charge sensor and as an electron reservoir. The highly regular coulomb peak spacing indicates a well-defined quantum dot, which has a constant charging energy of ∼0.9 meV. We extract a gate capacitance of 13 aF, in agreement with a simple parallel plate capacitor model. We form a double quantum dot between the

DOI: 10.1021/acs.nanolett.9b03254
Nano Lett. 2019, 19, 8653−8657

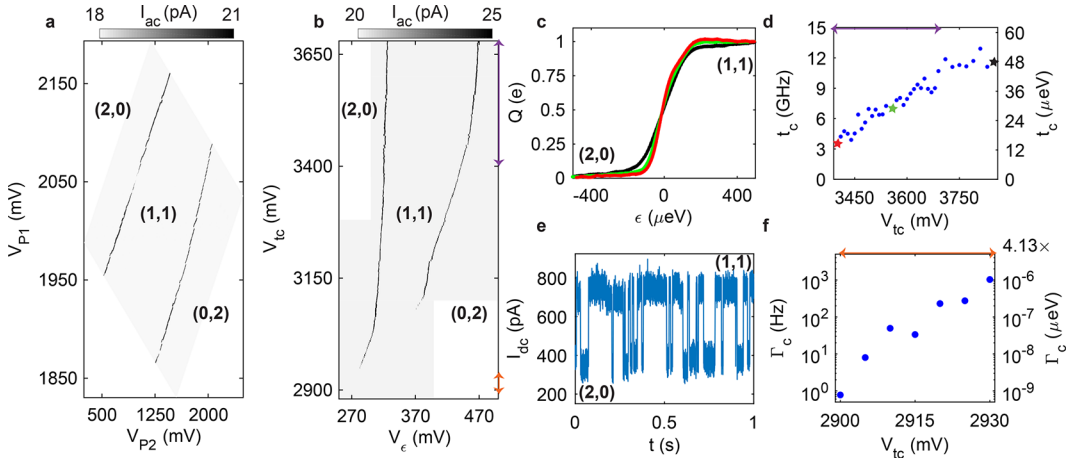

Figure 3. Charge stability diagrams and tunnel coupling control of an isolated double quantum dot. (a) Map of the isolated (2,0)-(1,1) and (1,1)-(0,2) anticrossings as a function of V_{P_2} and V_{P_1}. No additional electrons are loaded into the quantum dot islands due to a negligible Γ_R. (b) Map of the (2,0)-(1,1) and (1,1)-(0,2) anticrossings as a function of detuning and barrier voltage. The relative lever arm between V_{t_c} and V_ϵ changes at lower barrier voltages due to a change in quantum dot location. The orange and purple arrows indicate the ranges in which the tunnel coupling was determined using RTS and polarization line measurements, respectively. (c) Polarization lines (excess charge Q as a function of detuning ϵ) across the anticrossing for high t_c (black, V_{t_c} = 3.85 V), intermediate t_c (green, V_{t_c} = 3.6 V), and relatively low t_c (red, V_{t_c} = 3.4 V). (d) Extracted t_c from polarization lines as a function of V_{t_c}, where we find tunable t_c up to 13 GHz. (e) RTS for weak coupling V_{t_c} = 2.910 V. (f) Extracted Γ_c from RTS measurements as a function of V_{t_c}, demonstrating tunable tunnel rates down to <1 Hz.

confinement barriers CL and CR, using the gates P_1 and P_2 to tune the quantum dot potentials. B_t and B_R are used to control the tunnel coupling between the quantum dots and from the quantum dots to the SET, respectively.

We characterize the charge readout sensitivity by recording the RTS originating from the tunneling of the electrons between the (2,0) and (1,1) charge states with $\Gamma_c \approx 48$ Hz, where Γ_c is the interdot tunnel rate. The fidelity of the (2,0)-(1,1) charge readout is often limited by the sensitivity of the charge sensor to interdot transitions. We have designed and positioned the SET with respect to the double quantum dot in such a way that this sensitivity is maximized. Figure 1d shows a histogram of the measured readout signal using an integration time $\tau = 82$ μs. We fit the counts with a double Gaussian curve with $\mu_{(2,0),(1,1)}$ and $\sigma_{(2,0),(1,1)}$, the mean and standard deviations of the Gaussian distributions corresponding to the two charge states. We find that $\Delta\mu_{(2,0)-(1,1)} > 16\sigma_{(2,0)}$, corresponding to an excellent discrimination between the (2,0) and (1,1) charge states.

To precisely measure charge transitions, we implement charge sensing using a lock-in amplifier and apply a square-wave excitation at $f_{ac} = 77$ Hz on gate B_t. Figure 2a,b shows the double quantum dot charge stability diagrams of the charge sensor response as a function of V_{P_2} and V_{P_1} for weak ($V_{B_t} = 2.9$ V) and strong ($V_{B_t} = 3.6$ V) coupling. Horizontal and vertical blue lines indicate the loading of an additional electron from the SET to quantum dots D_1 (located under gate P_1) and D_2 (located under P_2), respectively, whereas diagonal yellow lines indicate electron transitions between the two quantum dots. We do not observe more charge transitions at voltages lower than the measured range (see Figure S1), and we conclude that the double quantum dot is in the single electron regime. To highlight the difference between weak and strong coupling, Figure 2c,d shows higher resolution maps of the (2,0)-(1,1) anticrossing.

When we set a weak interdot coupling, charge addition lines of D_2 are barely visible in the charge stability diagram because of the low tunnel rate between D_2 and the reservoir. This indicates that the tunnel rate is significantly smaller than the excitation frequency applied to the gate. Similarly, at the (2,0)-(1,1) interdot transition, no transitions between the quantum dots can be observed because of the low interdot coupling. The loading of the first electron in D_2 can only be observed from the shift of the D_1 charge addition line, caused by the mutual capacitance E_m of the two quantum dots. Only in the multielectron regime where the quantum dot wave functions are larger and have more overlap is the coupling sufficiently high to observe charge-transition lines.

When the interdot coupling is strong, charge addition lines belonging to D_2 are visible near the anticrossings and at high V_{P_1}, where Γ_{R_2} is increased. Additionally, t_c and E_m are increased, and we observe a honeycomb-shaped charge stability diagram with clearly visible interdot transition lines, even when only a single electron is loaded on each quantum dot.

We estimate the relative location and size of the quantum dots from the gate voltage differences $\Delta V_{P_{1(2)}}$ needed to load the second electron with respect to the first electron. We additionally use the cross-capacitances $\alpha_{r_{1(2)}}$ of the plunger gates, determined by measuring the shift in $V_{P_{1(2)}}$ of the charge-transition line of the first electron in $D_{1(2)}$ as a function of a step in $V_{P_{2(1)}}$, where $\alpha_{r_{1(2)}}$ is the ratio between the shift and the step.

When the coupling is weak, we find that $\Delta V_{P_1} \approx 70$ mV, $\alpha_{r_1} < 0.05$ for D_1 and $\Delta V_{P_2} \approx 50$ mV, $\alpha_{r_2} \approx 0.33$ for D_2. We conclude that we have a system of two weakly coupled quantum dots located under P_1 and P_2.

We now analyze how the locations of D_1 and D_2 change from the changes in ΔV_P and α_r. For D_1, both ΔV_{P_1} and α_{r_1} are almost independent of the coupling. For D_2, ΔV_{P_2} increases by a factor of 11, from $\Delta V_{P_2} \approx 50$ mV for weak coupling to $\Delta V_{P_2} \approx 550$ mV for strong coupling, whereas α_{r_2} increases by a factor of 5, from 0.3 to 1.5. The increase in α_{r_2} can be explained by a change in the

DOI: 10.1021/acs.nanolett.9b03254
Nano Lett. 2019, 19, 8653−8657

location of D_2 toward gate P_1 to a position partly below gate B_t. This change of quantum dot location will decrease the lever arm, and this is likely the cause of the increase in ΔV_{P_2}. We conclude that tuning from weak to strong coupling causes the location of D_2 to shift from a position mostly under P_2 to a position partly below B_t, whereas D_1 is stationary under P_1. The ease with which D_2 can be displaced additionally suggests that no unintentional quantum dots are formed between barrier gates.

By reducing V_{BR}, the tunnel rate Γ_R between the SET reservoir and the quantum dots can be reduced, and the loading and unloading of electrons can be prevented, resulting in an isolated quantum dot system.[27,34] Because the reservoir is connected to room-temperature electronics, decoupling the quantum dot from it may provide the advantage of reduced noise.[35] Figure 3a shows the (2,0)-(1,1) and (1,1)-(0,2) anticrossings as a function of V_{P_2} and V_{P_1} when the coupling is strong. Only interdot transition lines are present over a wide range of voltages, much larger than the ΔV_P extracted in the previous section. This implies that no additional electrons are loaded as a result of a negligible coupling to the reservoir. The ability to control the interdot transitions of a double quantum dot without loading additional electrons provides good prospects for the operation of quantum dot arrays that are only remotely coupled to reservoirs, as proposed in quantum information architectures.[17,19,20]

We control the tunnel coupling t_c with gate B_T. To compensate for the influence of V_{B_t} on detuning ϵ and on-site potential U, we implement virtual gates using a cross-capacitance matrix[9,36,37] and convert V_{P_2}, V_{P_1}, and V_{B_t} to ϵ, U, and t_c. Figure 3b shows the (2,0)-(1,1) and (1,1)-(0,2) anticrossings as a function of the new set of virtual gates, V_ϵ and V_{t_c}. For both transitions, the interdot line vanishes at low V_{t_c}, meaning that the coupling has been largely switched off. We observe that for the (1,1)-(0,2) anticrossing, the transition line disappears at $V_{t_c} < 3.1$ V, whereas for the (2,0)-(1,1) anticrossing, this happens for $V_{t_c} < 2.95$ V. The variation may come from a small asymmetry in the system.

We tune the double quantum dot to a significantly coupled regime and quantitatively analyze the system by taking charge polarization lines. Figure 3c shows charge polarization lines at high, intermediate, and relatively low tunnel couplings within this regime. We measure the charge sensor response Q as a function of detuning ϵ and fit the data according to a two-level model that includes cross-talk of ϵ to the charge sensor and the influence of the quantum dot charge state on the charge sensor sensitivity.[9,38] From the thermal broadening of the polarization line at low tunnel coupling, we extract the lever arm of V_ϵ for the detuning axis $\alpha_\epsilon \approx 0.04$ eV/mV by assuming the electron temperature to be equal to the fridge temperature of 0.44 K.

For relatively low tunnel couplings, we observe in the charge polarization lines deviations from the model for a two-level system[38] (see the red curve in Figure 3c with $\epsilon > 0$). This deviation can also not be explained by a modified model that includes valley states, considering an adiabatic detuning sweep and assuming zero temperature.[39] Whereas these measurements were done adiabatically, the elevated temperature of 0.44 K can cause a non-negligible population of a valley or other excited states. These excited states can cause a charge transition at a different detuning energy, thereby giving rise to a deviation. A large tunnel coupling can increase the relaxation rate of these excited states and thus decrease their population. As a consequence, the charge polarization lines are in agreement with the model for a two-level system[38] at larger tunnel couplings.

At tunnel couplings below 3 GHz, the thermal broadening of the polarization line prevents accurate fitting. Instead of the tunnel coupling energy t_c, we determine the interdot tunnel rate Γ_c, which is proportional to the square of the tunnel coupling.[40−42] We measure the RTS (Figure 3e) at the (2,0)-(1,1) transition and fit the counts C of a histogram of the tunnel times T to $C = Ae^{-\Gamma_c T}$, where A is a normalization constant. In the measurements, we have tuned V_ϵ such that $\Gamma_{c(2,0)\text{-}(1,1)} \approx \Gamma_{c(1,1)\text{-}(2,0)}$.

Figure 3d shows t_c as a function of V_{t_c}, demonstrating tunable tunnel coupling in the strong coupling regime, and Figure 3f shows the obtained Γ_c as a function of V_{t_c} from 1 kHz down to <1 Hz. We note that we can further reduce the tunnel rate to even smaller rates simply by further reducing V_{t_c}.

A change in the barrier height or width results in an exponential change in t_c and in Γ_c. When the tunnel coupling is low, D_2 is located mainly under P_2, and a change in V_{t_c} has a significant impact on the barrier. Correspondingly, we observe an exponential dependence of Γ_c versus V_{t_c}. When the tunnel coupling is high, D_2 is located mostly under B_t, and the impact of V_{t_c} on the barrier is vanishing. As a result, we observe a seemingly linear dependence of t_c versus V_{t_c} from 3 up to 11 GHz that saturates ~13 GHz for $V_{t_c} > 3675$ mV.

In conclusion, we have demonstrated control over the tunnel coupling of single electrons residing in a double quantum dot in SiMOS. The interdot coupling of the (2,0)-(1,1) charge transition can be controlled by a barrier gate that changes the quantum dot location. We have demonstrated control over the tunnel coupling in the strong coupling regime from 3 to 13 GHz as well as control over the tunnel rate in the weak coupling regime from 1 kHz to <1 Hz. Achieving this degree of control in an isolated system constitutes a crucial step toward independent control over detuning and tunnel coupling for the operation at the charge symmetry point[5,6] and reaching the control required for large-scale quantum computation with quantum dots.[1,17−22] Whereas SiMOS systems are often said to be severely limited by disorder, the excellent control shown here provides great prospects to operate larger arrays fabricated using conventional semiconductor technology.

■ ASSOCIATED CONTENT

Supporting Information

The Supporting Information is available free of charge at https://pubs.acs.org/doi/10.1021/acs.nanolett.9b03254.

Figure S1. Charge stability diagram as a function of V_{Bt} and V_{P1}, confirming that both quantum dots can be fully depleted (PDF)

■ AUTHOR INFORMATION

Corresponding Author

*E-mail: m.veldhorst@tudelft.nl.

ORCID

L. Petit: 0000-0001-9877-3623

W. I. L. Lawrie: 0000-0002-9946-4117

Author Contributions

§H.G.J.E. and L.P. contributed equally to this work.

DOI: 10.1021/acs.nanolett.9b03254
Nano Lett. 2019, 19, 8653−8657

Notes

The authors declare no competing financial interest.

■ ACKNOWLEDGMENTS

We thank Max Russ for helpful discussions. H.G.J.E, L.P., and M.V. are funded by a Netherlands Organization of Scientific Research (NWO) VIDI grant. Research was sponsored by the Army Research Office (ARO) and was accomplished under grant no. W911NF-17-1-0274. The views and conclusions contained in this document are those of the authors and should not be interpreted as representing the official policies, either expressed or implied, of the Army Research Office (ARO), or the U.S. Government. The U.S. Government is authorized to reproduce and distribute reprints for Government purposes notwithstanding any copyright notation herein.

■ REFERENCES

(1) Loss, D.; DiVincenzo, D. P. *Phys. Rev. A: At., Mol., Opt. Phys.* **1998**, *57*, 120.
(2) Levy, J. *Phys. Rev. Lett.* **2002**, *89*, 147902.
(3) DiVincenzo, D. P.; Bacon, D.; Kempe, J.; Burkard, G.; Whaley, K. B. *Nature* **2000**, *408*, 339.
(4) Shi, Z.; Simmons, C. B.; Prance, J. R.; Gamble, J. K.; Koh, T. S.; Shim, Y.-P.; Hu, X.; Savage, D. E.; Lagally, M. G.; Eriksson, M. A.; et al. *Phys. Rev. Lett.* **2012**, *108*, 140503.
(5) Martins, F.; Malinowski, F. K.; Nissen, P. D.; Barnes, E.; Fallahi, S.; Gardner, G. C.; Manfra, M. J.; Marcus, C. M.; Kuemmeth, F. *Phys. Rev. Lett.* **2016**, *116*, 116801.
(6) Reed, M. D.; Maune, B. M.; Andrews, R. W.; Borselli, M. G.; Eng, K.; Jura, M. P.; Kiselev, A. A.; Ladd, T. D.; Merkel, S. T.; Milosavljevic, I.; et al. *Phys. Rev. Lett.* **2016**, *116*, 110402.
(7) Taylor, J. M.; Srinivasa, V.; Medford, J. *Phys. Rev. Lett.* **2013**, *111*, 050502.
(8) Kim, D.; Shi, Z.; Simmons, C. B.; Ward, D. R.; Prance, J. R.; Koh, T. S.; Gamble, J. K.; Savage, D. E.; Lagally, M. G.; Friesen, M.; et al. *Nature* **2014**, *511*, 70.
(9) Hensgens, T.; Fujita, T.; Janssen, L.; Li, X.; Van Diepen, C. J.; Reichl, C.; Wegscheider, W.; Das Sarma, S.; Vandersypen, L. M. K. *Nature* **2017**, *548*, 70.
(10) Borselli, M. G.; Eng, K.; Ross, R. S.; Hazard, T. M.; Holabird, K. S.; Huang, B.; Kiselev, A. A.; Deelman, P. W.; Warren, L. D.; Milosavljevic, I.; et al. *Nanotechnology* **2015**, *26*, 375202.
(11) Zajac, D. M.; Sigillito, A. J.; Russ, M.; Borjans, F.; Taylor, J. M.; Burkard, G.; Petta, J. R. *Science* **2018**, *359*, 439−442.
(12) Hendrickx, N. W.; Franke, D. P.; Sammak, A.; Kouwenhoven, M.; Sabbagh, D.; Yeoh, L.; Li, R.; Tagliaferri, M. L. V.; Virgilio, M.; Capellini, G.; et al. *Nat. Commun.* **2018**, *9*, 2835.
(13) Hendrickx, N. W.; Franke, D. P.; Sammak, A.; Scappucci, G.; Veldhorst, M. Fast Two-Qubit Logic with Holes in Germanium. 2019, arXiv:1904.11443. arXiv.org e-Print archive. https://arxiv.org/abs/1904.11443 (accessed November 7, 2019).
(14) Sabbagh, D.; Thomas, N.; Torres, J.; Pillarisetty, R.; Amin, P.; George, H.; Singh, K.; Budrevich, A.; Robinson, M.; Merrill, D.; et al. *Phys. Rev. Appl.* **2019**, *12*, 014013.
(15) Mazzocchi, V.; Sennikov, P.; Bulanov, A. D.; Churbanov, M. F.; Bertrand, B.; Hutin, L.; Barnes, J. P.; Drozdov, M. N.; Hartmann, J. M.; Sanquer, M. *J. Cryst. Growth* **2019**, *509*, 1−7.
(16) Maurand, R.; Jehl, X.; Kotekar-Patil, D.; Corna, A.; Bohuslavskyi, H.; Laviéville, R.; Hutin, L.; Barraud, S.; Vinet, M.; Sanquer, M.; et al. *Nat. Commun.* **2016**, *7*, 13575.
(17) Veldhorst, M.; Eenink, H. G. J.; Yang, C. H.; Dzurak, A. S. *Nat. Commun.* **2017**, *8*, 1766.
(18) Vandersypen, L. M. K.; Bluhm, H.; Clarke, J. S.; Dzurak, A. S.; Ishihara, R.; Morello, A.; Reilly, D. J.; Schreiber, L. R.; Veldhorst, M. *npj Quantum Inf.* **2017**, *3*, No. 34.
(19) Li, R.; Petit, L.; Franke, D. P.; Dehollain, J. P.; Helsen, J.; Steudtner, M.; Thomas, N. K.; Yoscovits, Z. R.; Singh, K. J.; Wehner, S.; et al. *Sci. Adv.* **2018**, *4*, No. eaar3960.
(20) Taylor, J. M.; Engel, H.-A.; Dür, W.; Yacoby, A.; Marcus, C. M.; Zoller, P.; Lukin, M. D. *Nat. Phys.* **2005**, *1*, 177.
(21) Friesen, M.; Biswas, A.; Hu, X.; Lidar, D. *Phys. Rev. Lett.* **2007**, *98*, 230503.
(22) Trauzettel, B.; Bulaev, D. V.; Loss, D.; Burkard, G. *Nat. Phys.* **2007**, *3*, 192.
(23) Veldhorst, M.; Yang, C. H.; Hwang, J. C. C.; Huang, W.; Dehollain, J. P.; Muhonen, J. T.; Simmons, S.; Laucht, A.; Hudson, F. E.; Itoh, K. M.; et al. *Nature* **2015**, *526*, 410−414.
(24) Huang, W.; Yang, C. H.; Chan, K. W.; Tanttu, T.; Hensen, B.; Leon, R. C. C.; Fogarty, M. A.; Hwang, J. C. C.; Hudson, F. E.; Itoh, K. M.; et al. *Nature* **2019**, *569*, 532−536.
(25) Tracy, L. A.; Nordberg, E.; Young, R.; Borras Pinilla, C.; Stalford, H.; Ten Eyck, G. A.; Eng, K.; Childs, K. D.; Wendt, J. R.; Grubbs, R. K.; et al. *Appl. Phys. Lett.* **2010**, *97*, 192110.
(26) Lai, N. S.; Lim, W. H.; Yang, C. H.; Zwanenburg, F. A.; Coish, W. A.; Qassemi, F.; Morello, A.; Dzurak, A. S. *Sci. Rep.* **2011**, *1*, No. 110.
(27) Yang, C. H.; Leon, R. C. C.; Hwang, J. C. C.; Saraiva, A.; Tanttu, T.; Huang, W.; Lemyre, J. C.; Chan, K. W.; Tan, K. Y.; Hudson, F. E.; et al. Silicon Quantum Processor Unit Cell Operation above One Kelvin. 2019, arXiv:1902.09126. arXiv.org e-Print archive. https://arxiv.org/abs/1902.09126 (accessed November 7, 2019).
(28) Veldhorst, M.; Hwang, J. C. C.; Yang, C. H.; Leenstra, A. W.; de Ronde, B.; Dehollain, J. P.; Muhonen, J. T.; Hudson, F. E.; Itoh, K. M.; Morello, A.; et al. *Nat. Nanotechnol.* **2014**, *9*, 981−985.
(29) Angus, S. J.; Ferguson, A. J.; Dzurak, A. S.; Clark, R. G. *Nano Lett.* **2007**, *7*, 2051−2055.
(30) Zajac, D.; Hazard, T.; Mi, X.; Nielsen, E.; Petta, J. R. *Phys. Rev. Appl.* **2016**, *6*, 054013.
(31) Brauns, M.; Amitonov, S. V.; Spruijtenburg, P. C.; Zwanenburg, F. A. *Sci. Rep.* **2018**, *8*, 5690.
(32) Kim, J. S.; Tyryshkin, A. M.; Lyon, S. A. *Appl. Phys. Lett.* **2017**, *110*, 123505.
(33) Nordberg, E. P.; Ten Eyck, G. A.; Stalford, H. L.; Muller, R. P.; Young, R. W.; Eng, K.; Tracy, L. A.; Childs, K. D.; Wendt, J. R.; Grubbs, R. K.; et al. *Phys. Rev. B* **2009**, *80*, 115331.
(34) Bertrand, B.; Flentje, H.; Takada, S.; Yamamoto, M.; Tarucha, S.; Ludwig, A.; Wieck, A. D.; Bäuerle, C.; Meunier, T. *Phys. Rev. Lett.* **2015**, *115*, 096801.
(35) Rossi, A.; Ferrus, T.; Williams, D. A. *Appl. Phys. Lett.* **2012**, *100*, 133503.
(36) Baart, T. A.; Shafiei, M.; Fujita, T.; Reichl, C.; Wegscheider, W.; Vandersypen, L. M. K. *Nat. Nanotechnol.* **2016**, *11*, 330.
(37) Mills, A.; Zajac, D.; Gullans, M.; Schupp, F.; Hazard, T.; Petta, J. R. *Nat. Commun.* **2019**, *10*, 1063.
(38) DiCarlo, L.; Lynch, H. J.; Johnson, A. C.; Childress, L. I.; Crockett, K.; Marcus, C. M.; Hanson, M. P.; Gossard, A. C. *Phys. Rev. Lett.* **2004**, *92*, 226801.
(39) Zhao, X.; Hu, X. Coherent Electron Transport in Silicon Quantum Dots. 2018, arXiv:1803.00749. arXiv.org e-Print archive. https://arxiv.org/abs/1803.00749 (accessed November 7, 2019).
(40) Braakman, F. R.; Barthelemy, P.; Reichl, C.; Wegscheider, W.; Vandersypen, L. M. K. *Nat. Nanotechnol.* **2013**, *8*, 432.
(41) Gamble, J. K.; Friesen, M.; Coppersmith, S. N.; Hu, X. *Phys. Rev. B: Condens. Matter Mater. Phys.* **2012**, *86*, 035302.
(42) Korotkov, A. N. *Phys. Rev. B: Condens. Matter Mater. Phys.* **1999**, *60*, 5737.

DOI: 10.1021/acs.nanolett.9b03254
Nano Lett. 2019, 19, 8653−8657